Electronic Supplementary Information

Monitoring surface transformations of metal carbodiimide water oxidation catalysts by *operando* XAS and Raman spectroscopy

Rafael Müller, Jinggang Lan, Karla Lienau, René Moré, C. A. Triana, Marcella Iannuzzi and Greta R. Patzke

University of Zurich, Department of Chemistry, Winterthurerstrasse 190, CH-8057 Zurich, Switzerland

CONTENTS

1 SYNTHETIC METHODS

The synthesis of the transition metal carbodiimides MNCN (M = Co, $Co_{0.9}Ni_{0.1}$, Ni, Mn, Cu) was adapted following the literature protocols described by Krott et al.[1–4], Ressnig et al.[5–7] and Koziej et al.[8] For the metals investigated in this study the precipitation method with ammonium carbonate was found to be most straightforward and to afford smaller particle sizes below 10 µm that are favourable for catalytic applications. MnNCN and CuNCN were obtained in one step, while Co and Ni salts form hydrogencyanamide precursors ($M(HNCN)_2$) that are subjected to thermal decomposition. Careful exclusion of oxygen and water is required, especially in the decomposition step of the precursors in salt melts, to avoid formation of metal oxide impurities. During heating of the $M(HNCN)_2$ precursors to 400 °C mainly melamine ($C_3H_6N_6$) is produced by trimerization of cyanamide. While this side product sublimates from the molten eutectic-salt, it can also undergo parallel polycondensation reactions (by elimination of NH_3) via melem ($C_6H_6N_{10}$) and further steps ($C_{3n}N_{(4-5)n}H_{(0-3)n}$, n>2) up to the formation of graphitic C_3N_4. Lowering the pressure in this step helps to avoid formation of insoluble polymeric carbon nitrides by faster removal of melamine. The following details describe the individual procedures used to obtain the different MNCN materials investigated in this study.

1.1 CoNCN

1.1.1 Synthesis of $Co(HNCN)_2$

$CoCl_2$ (1 mmol) was heated in cyanamide (30 mmol) to 75 °C until it was completely dissolved. Next, $(NH_4)_2CO_3$ (2 mmol) was added under stirring. After addition of deionized water the precipitate was separated by centrifugation and dried.

1.1.2 Synthesis of CoNCN

A mixture of 93 mg $Co(NCNH)_2$ (0.66 mmol) and 2.4 g LiCl-KCl eutectic salt (50:50 wt%) was dried in a in two-neck round-bottom flask under vacuum at 50-80 °C for 8 h. The mixture was then heated to 400 °C under N_2 for 2.5 h. The temperature was controlled using a heating mantle and a thermal sensor introduced into the mixture through a septum. After cooling to room temperature the salt cake was dissolved in deionized water and the solid product was collected by filtration. The product was washed with deionized water and dried in air.

1.1.3 $Co_{0.9}Ni_{0.1}NCN$

0.23 g $CoCl_2$ (1.8 mmol) and 26 mg $NiCl_2$ (0.2 mmol) were heated to 75°C in 2.5 g cyanamide (60 mmol).
0.38 g $(NH_4)_2CO_3$ (4 mmol) were added to the stirred solution. After addition of deionized water the product $Co_{0.9}Ni_{0.1}(HNCN)_2$ was separated by filtration and dried in air. $Co_{0.9}Ni_{0.1}NCN$ was obtained via the same thermal decomposition route as described in 1.1.2.

1.1.4 NiNCN

5 mmol $NiCl_2·6\,H_2O$ and 26 mmol cyanamide were dissolved in 20 ml 12.5% NH_3. After stirring overnight, further NH_3 and cyanamide were added until a blue solution was formed. This was left to crystallize and was filtered subsequently to collect a green precipitate. $Ni(NCNH)_2$ powder was obtained in both filtrations as confirmed by PXRD (Fig. 2, main text).
630 mg $Ni(NCNH)_2$ (4.5 mmol) were dried in 13 g LiCl-KCl eutectic salt (50:50 wt%) in a in two-neck round-bottom flask under vacuum at room temperature for 30 min. For the second step see 1.1.2.

1.1.5 MnNCN

$MnCl_2$ (4 mmol) and cyanamide (120 mmol) were used in the same precipitation procedure with $(NH_4)CO_3$ as described above (see 1.1.1) and directly afforded MnNCN. PXRD measurements showed low crystallinity, but no manganese oxide side product peaks (Fig. 2, main text).

1.1.6 CuNCN

$CuCl_2$ (4 mmol) and cyanamide (120 mmol) were used in the same procedure as above (see 1.1.1) while heating to 65°C and CuNCN was obtained by filtration.

2 CATALYST INK PREPARATION

5 mg MNCN were gently ground in an agate mortar and mixed with 42.2 µL Nafion (5% solution, Aldrich) and 320 µL ethanol.

2.1 Screen printed electrode modification

Screen printed electrodes (SPEs) (Fig. S1) with working electrode (WE) area diameter of 4 mm were coated by dropcasting the corresponding inks that had been sonicated for 10 min. An electrode loading series was prepared with 1, 5 and 10 µL ink. The dropcasted volumes resulted in the following coverages of the SPE-WE area: 1 µL (partial coverage), 5 µL (full coverage), 10 µL (excess coverage). Another series of electrodes was prepared by careful manual application of ink until a thin apparent monolayer of particles was achieved using 1.5 to 2.0 µL ink.

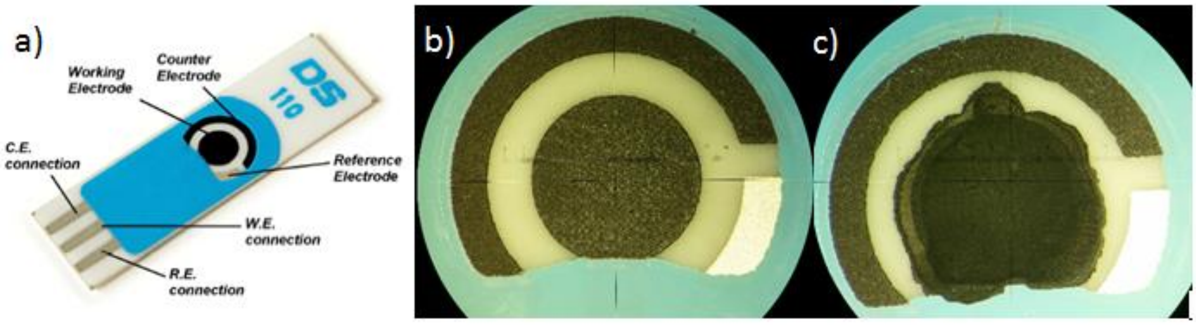

Fig. S1. (a) Screen printed electrode (SPE) layout.[a] (b) Pristine uncoated electrode. (c) Electrode surface coated by dropcasting 2 µL CoNCN/Nafion ink.

2.2 Screen printed electrode chronoamperometry

Ex situ chronoamperometry experiments were conducted by a stepwise (180 s) increase of the potential in the range of 0.3 - 1.0 V versus Ag/AgCl. The experiment was done with 2 µL ink loaded SPEs in 0.1 M KOH electrolyte with a glassy carbon counter electrode. For the catalytically active carbodiimides the procedure was repeated with new electrodes and 600 s steps up to 1.2 V vs. Ag/AgCl.

Additional chronoaperometry was performed with the SPE droplet microvolume setup (50 µL electrolyte) as used for the operando experiments. ^{18}O labelled water was used for electrolyte preparation und the SPEs were inserted in a septum sealed glass vial to minimize atmospheric moisture exchange. The post catalytic Raman spectra are compared in Fig. S9. Attempts of Raman coupled operando voltammetry by covering the SPE with a thin glass slide (5 µL electrolyte microlayer) did not provide optimal results, because the current density was observed to decrease quickly and the Raman focus was disturbed as soon as gas evolution set in.

---

[a] http://www.dropsens.com/en/screen_printed_electrodes_pag.html

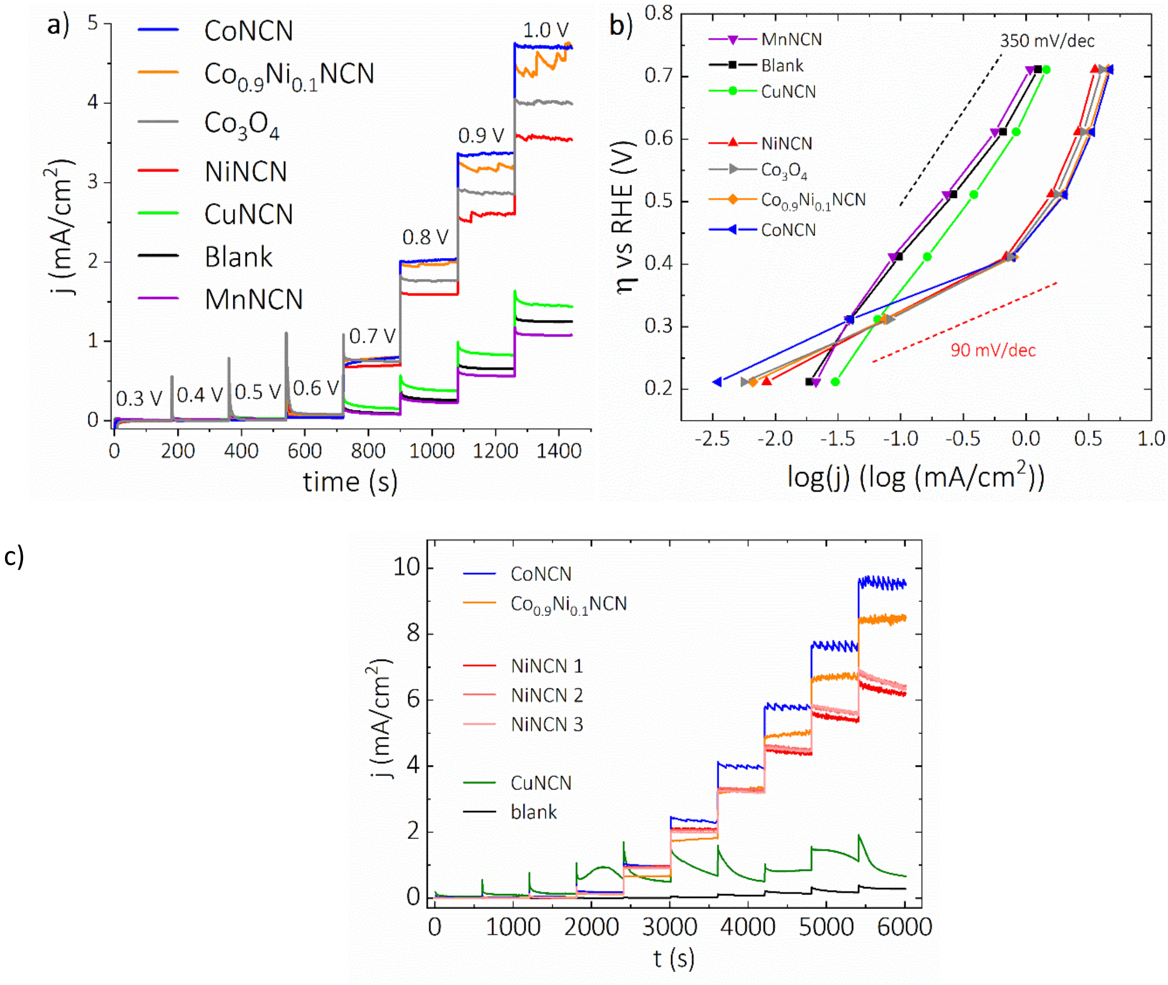

Fig. S2. (a) Chronoamperometry response of MNCN modified SPEs reproduced in a conventional 3-electrode setup. Current fluctuations in the CP steps are caused by oxygen bubble formation and their release. (b) Representation as Tafel plot. (c) Extended duration (600 s per step) and potential range (0.3 – 1.2 V vs. Ag/AgCl, 1.242 – 2.142 V vs. RHE, 12 – 912 mV η) chronoamperometry response of the active MNCN modified SPEs reproduced as shown in (a). Clearly irregular current is observed for CuNCN indicating transformations involving redox-active species and possibly chemical reaction steps. NiNCN shows lower and decreasing current compared to the Co-based carbodiimides. Consecutive chronoamperometry experiments with the same NiNCN electrode reproduce the current decrease consistently in each step but show no persistent activity loss.

3 RRDE VOLTAMMETRY

The dimensions of the RRDE used are as follows: GC disc (r = 2.5 mm, Ø = 5 mm), 375 µm gap, Pt ring (width = 375 µm, r_{inner} = 2.875 mm, r_{outer} = 3.250 mm, $Ø_{inner}$ = 5.750 mm, $Ø_{outer}$ = 6.500 mm). With this geometry the theoretical collection efficiency N for the bare uncoated RRDE was calculated to be 25.01% using Equation 1. The literature value from the distributor Metrohm is 24.9% and the experimental determination with $K_4[Fe(CN)_6]$ as standard and blank measurements afforded a value of 24.75% ± 0.25% with a linear response region from 400 to 2000 rpm. Due to the change of surface topology of the GC disc by the coating layer the rotational electrolyte flow becomes more turbulent and the real mass transport dynamics consequently deviate from the theoretical model. Therefore, the real collection efficiency is lowered and its correlation to the square root of rotation speed deviates from ideal linearity. Nevertheless it remains constant for similar electrodes, in this case 17%, and it is independent of the applied potential. This allows comparison of the ratio of corresponding disc and ring currents attributed to water oxidation and oxygen reduction in contrast to irreversible and surface confined side reactions.

$$N_{theoretical} = 1 - \sigma_{OD}^{2} + \sigma_{B}^{\frac{2}{3}} - G(\sigma_C) - \sigma_{B}^{\frac{2}{3}} G(\sigma_A) + \sigma_{OD}^{2} G(\sigma_C\, \sigma_{OD}^{3}) \quad (1)$$

Equation 1: Theoretical collection efficiency.[9]

4 *EX SITU* VIBRATIONAL SPECTROSCOPY

4.1 *Ex situ* Raman spectroscopy

Ex situ Raman spectra collected using different excitation wavelengths (532, 633 and 785 nm) exhibit qualitatively similar peaks which differ only with respect to backgrounds and intensities (see Fig. S3). The excitation wavelength of the 532 nm laser was selected for *ex situ* experiments due to its optimal signal to noise ratio. Under *operando* conditions the 785 nm laser was favoured due to lower fluorescence.

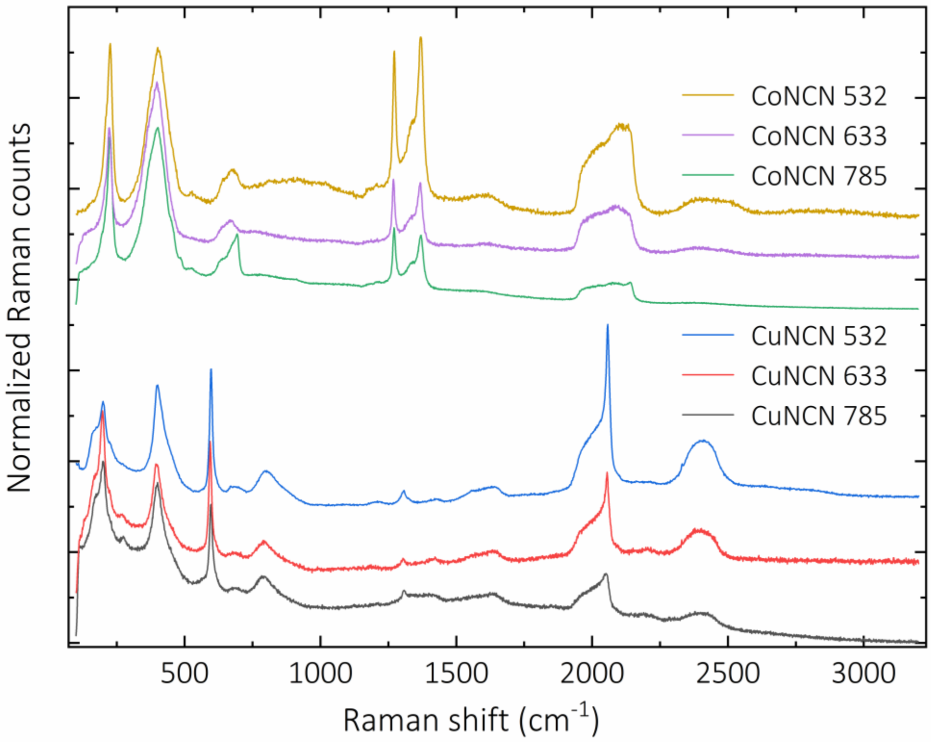

Fig. S3. *Ex situ* Raman spectra recorded with different excitation wavelengths. Spectra acquisitions with 633 and 785 nm wavelengths require increasing accumulation times (up to 8 h).

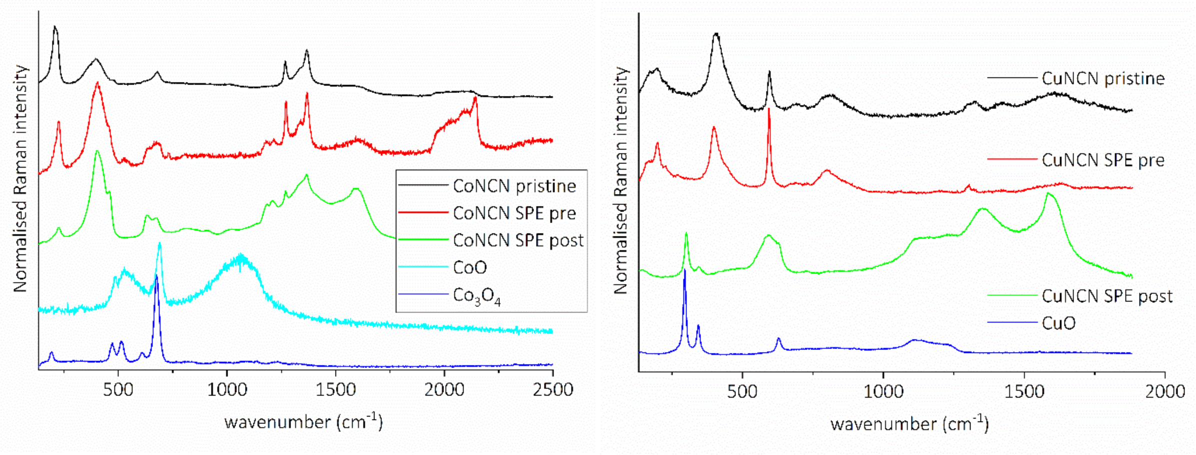

Fig. S4. Raman spectra comparison of pristine MNCN powders and pre- and post-catalytic SPEs vs. oxide references.

4.2 *Ex situ* FT-IR spectroscopy

The experimental MNCN (M = Mn, Co, Ni) FT-IR spectra show additional vibrations between 1100 cm^{-1} and 1700 cm^{-1} due to the overlapping peaks of side products. These can most likely be attributed to cyanamide polymerization for MnNCN and CuNCN and melamine polycondensation ($C_{3n}N_{(4-5)n}H_{(0-3)n}$ with $n > 2$) for CoNCN and NiNCN (Fig. S5). The very weak signals above 3000 cm^{-1} can either result from the same side products or from combinational NCN modes ($\nu_s + \nu_{as}$ = 3203-3211 cm^{-1}).

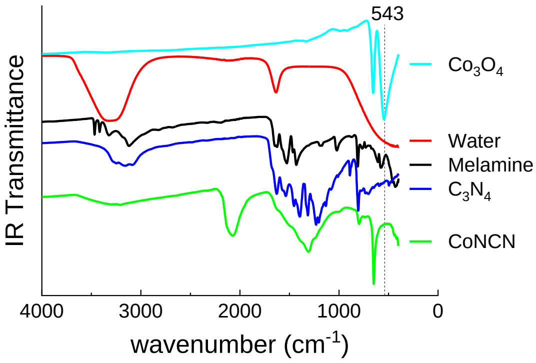

Fig. S5. Comparison of FT-IR spectra of typical impurities with CoNCN as a representative carbodiimide showing residual side product peaks of the N-C vibrations of the cyanamide condensation products melamin, melem and carbon nitride (g-C_3N_4) at 800 cm^{-1} and broad overlapping absorption from 1000-1700 cm^{-1}. Co_3O_4 (543 cm^{-1}) peaks are absent in pristine CoNCN.

4.3 Analysis of dissolution and etching phenomena

The leaching stability was evaluated by stirring pristine MNCN samples for 20 h in 1.0 M or 0.1 M KOH, followed by centrifugation, washing, and filtration (0.22 micron filter). Spectroscopic and PXRD investigations of the obtained solids and comparisons with the respective pristine materials show no significant oxide formation after exposure to basic conditions (see Figs. S6-S8).

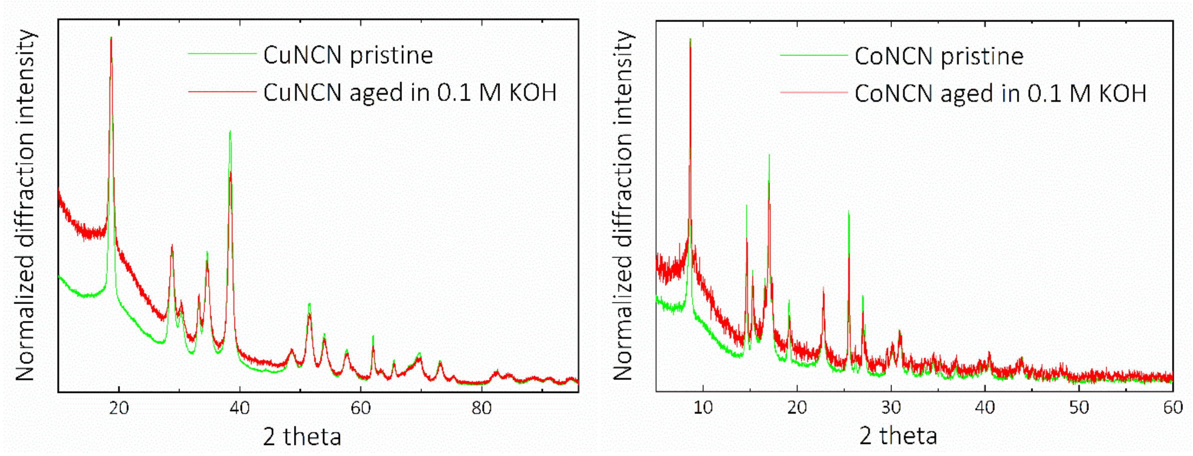

Fig. S6. Powder XRD patterns before and after aging of CoNCN and CuNCN samples in 0.1 M KOH (CuNCN: Cu-K_α radiation; CoNCN: Mo-K_α radiation) vs. reference patterns of pristine MNCN compounds.

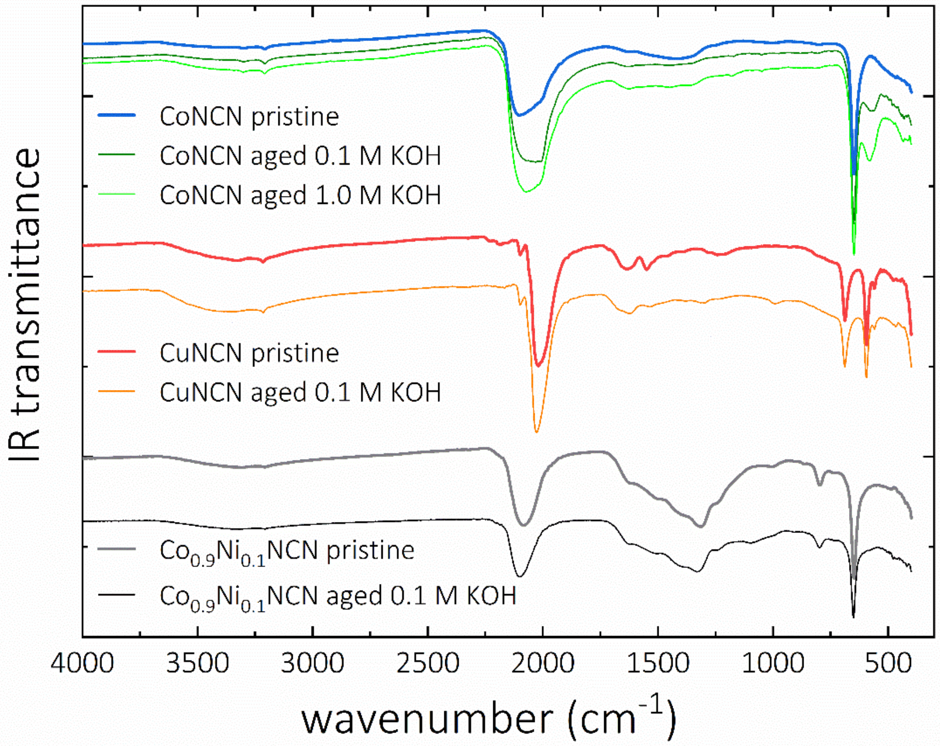

Fig. S7. FT-IR spectra of CoNCN, CuNCN and $Co_{0.9}Ni_{0.1}NCN$ before and after ageing in KOH. The only additional feature arising in post-treatment spectra is a small peak at ca. 570 cm^{-1} for CoNCN. This does not match with CoO or $Co(OH)_2$ nor with Co_3O_4 showing absorptions at 550 cm^{-1} and 640 cm^{-1}. Overlap of the latter signal is unlikely given that no peak shift was observed for the NCN deformation mode peaks of CoNCN (650 cm^{-1}).

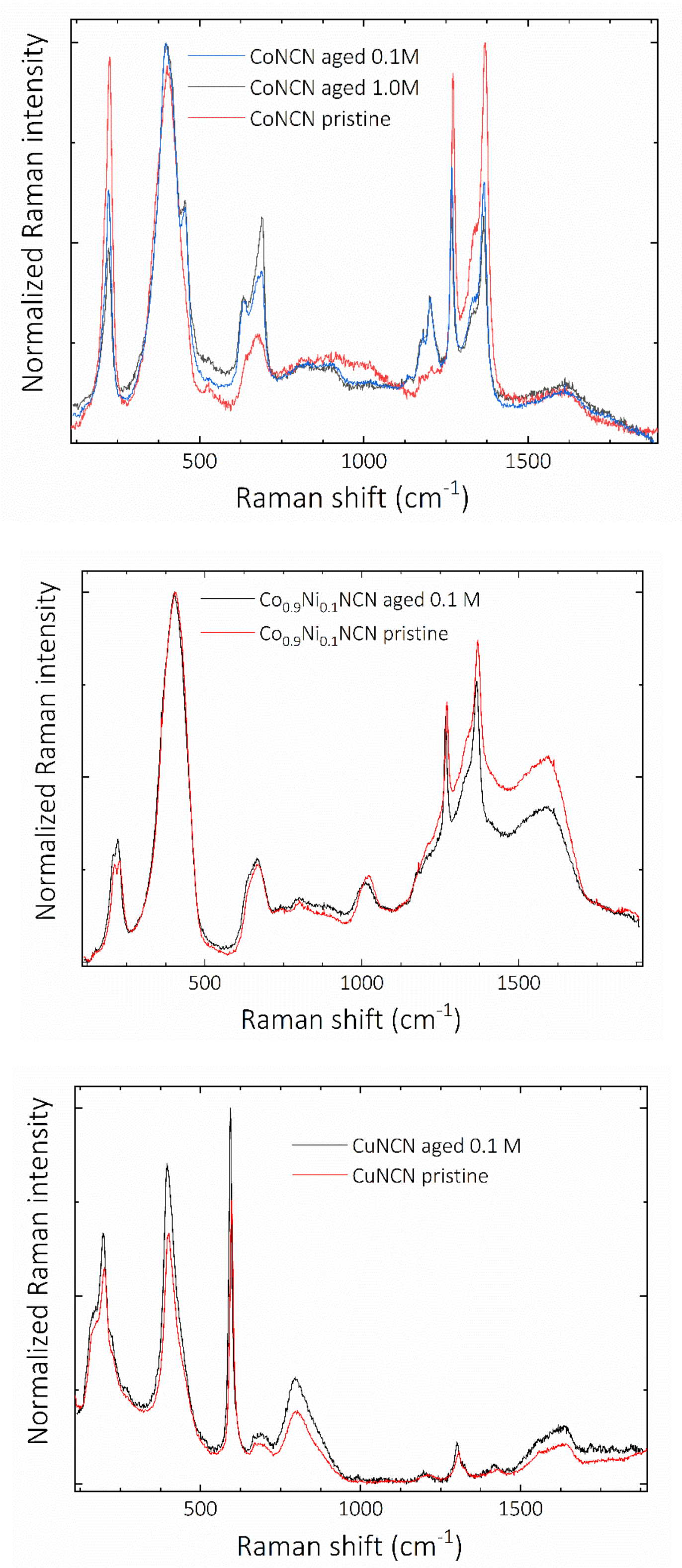

Fig. S8. Raman spectra of CoNCN, CuNCN and $Co_{0.9}Ni_{0.1}NCN$ before and after ageing in KOH. Relative peak intensity changes have been observed to depend on crystallinity and orientation of the crystallites. The small feature at 1200 cm^{-1} in the spectrum of CoNCN may indicate low amounts of NCN in cyanamide configuration.

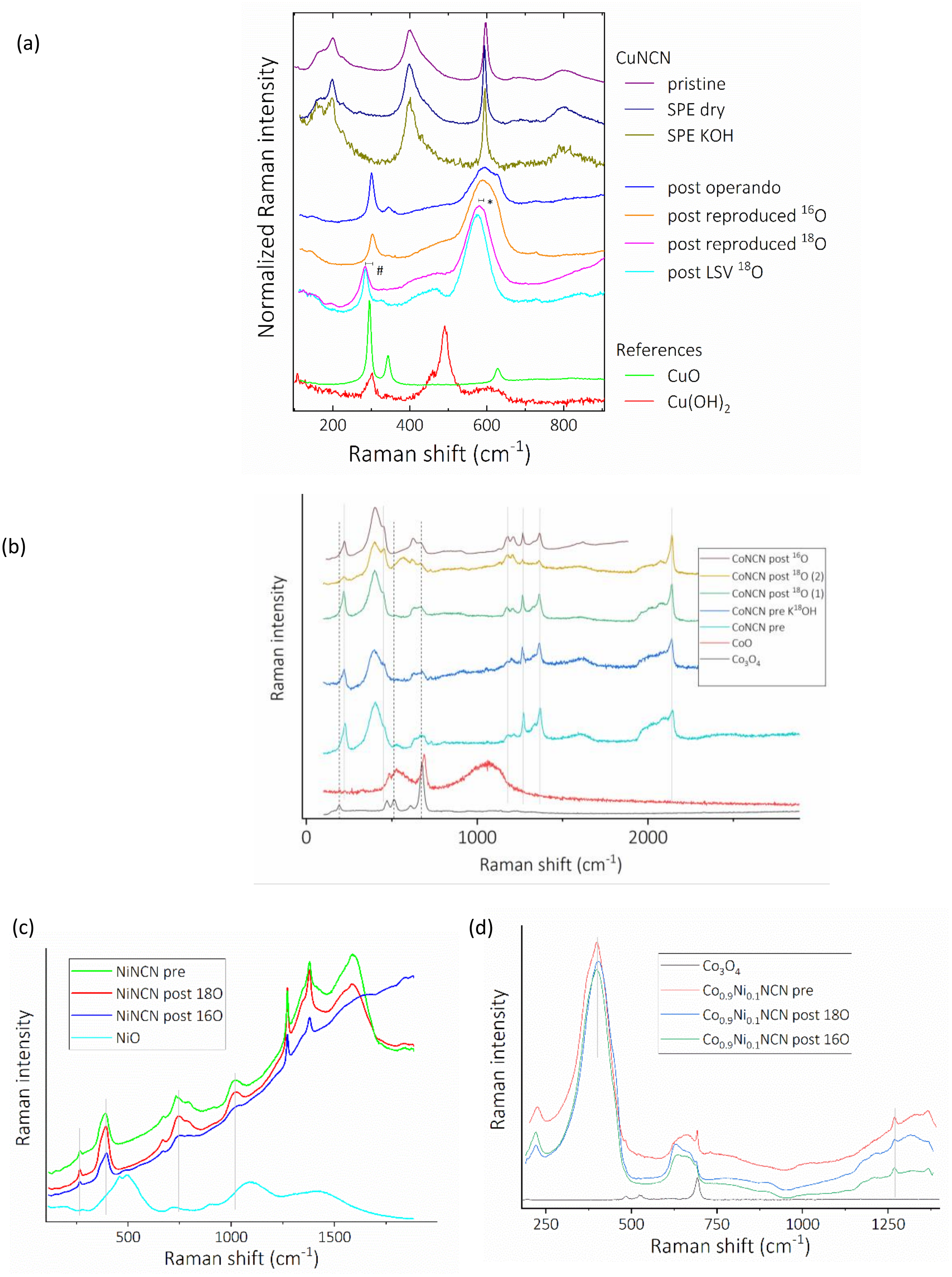

Fig. S9. Representative averages of Raman mappings showing the peak shift (Δv) induced by using 97% ^{18}O enriched water (grey lines = optical guidelines) for (a) electrocatalytic tests with CuNCN (# indicates Δv = 15 cm^{-1} (calculated 17 cm^{-1}), * indicates Δv = 13 cm^{-1} (calculated 34 cm^{-1})). Comparison of dry catalyst layer and electrolyte covered catalyst layer show no significant change other than a reduced signal amplitude and rising scattering background below 200 cm^{-1} caused by KOH. Representative averages of Raman mappings (b) CoNCN SPEs, (c) NiNCN SPEs and (d) $Co_{0.9}Ni_{0.1}NCN$ SPEs, all after electroanalytical procedures in normal and isotope enriched electrolyte.

CoNCN (Fig. S9b): No oxide peaks arise and no peak-shift occurs in any of the measurements. Careful inspection of several samples suggests that the intensity of the shoulder at 460 cm^{-1} appears to increase as well as of the peaks around 1200 cm^{-1} below the symmetric stretching vibration. The latter are usually found in pristine material only very weak or hidden as shoulders (cf. Fig. S8). They are visible on the pre-catalytic layer without electrolyte (light blue), increase slightly in contact with electrolyte (dark blue) and appear to be more pronounced after catalysis (green, orange, and brown). This trend suggests a correlation with the duration of exposure to aqueous solutions. A plausible hypothesis is the formation of the cyanamide form of NCN on the surface by protonation or hydrolysis. The NCN symmetric stretching vibration is found in this region of Raman shifts for H_2NCN (1152 cm^{-1}) as well as those of other metal-NCN species with N-C-N angles deviating from 180°.[10] Furthermore, no oxygen involvement is indicated for this signal as seen by the absence of an isotope shift (orange and brown trace).

NiNCN (Fig. S9c): No significant peak shift is observed among the measurement series.

$Co_{0.9}Ni_{0.1}NCN$ (Fig. S9d): No peaks shifts are observed after exposure to ^{18}O either. (The very low intensity impurity peak around 700 cm^{-1} was only observed for a specific spot of the sample during the mappings. It might thus be an artefact of local thermal Raman laser damage, especially given that it is barely discernible in the post-electrocatalytic samples any more and does not exhibit an ^{18}O induced shift.)

4.4 Phonon calculations

Density function theory (DFT) was implemented using the CP2K package.[11] Calculations were carried out into the Kohn-Sham formalism involving Gaussian and Plane Waves based methods.[12,13] The Goedecker-Teter-Hutter (GTH) pseudopotentials[11,14] and the DZVP-MOLOPT-GTH basis sets[13] were used to describe the molecules with a plane wave energy cut-off of 500 Ry. The vibrational spectra of bulk CoNCN were calculated by ab-initio molecular dynamics (AIMD) simulations. Calculations were implemented at 300 K using the Nose-Hoover chain thermostat[15,16] with a time step of 0.5 fs in the canonical ensemble (NVT). The system was equilibrated for 5 ps, and then allowed to evolve for 10 ps. The power and IR vibrational spectra were calculated by means of the mass-weighted velocity autocorrelation function and dipole moment autocorrelation function as implemented in the TRAVIS program[17,18] and defined respectively according to:

$$P(\omega) = m \int \langle \dot{r}(\tau)\dot{r}(t+\tau)\rangle_\tau \mathrm{e}^{-i\omega t}\mathrm{d}t, \tag{2}$$

$$A(\omega) \propto m \int \langle \dot{\mu}(\tau)\dot{\mu}(t+\tau)\rangle_\tau \mathrm{e}^{-i\omega t}\mathrm{d}t. \tag{3}$$

The calculated atomic contribution to the vibrations and the directions of displacement match the expectation from well-known molecular NCN vibrations (above 500 cm^{-1}) very well, indicating acceptable calculated results. See Fig. S10. The lattice phonons appear at lower wavenumbers, involve Co and are dominated by atom displacement in the *ab*-plane, see Fig. S11.

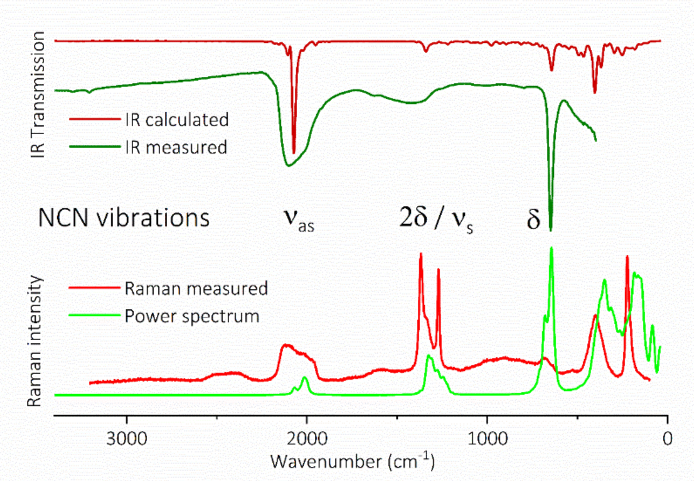

Fig. S10. Comparison of experimental and calculated vibrational spectra for CoNCN. Alignment of experimentally observed frequencies is achieved by a scale shift of 42 cm^{-1}, which is acceptable as the absolute energy scale resulting from theoretical approaches frequently contains uncertainties in the same order of magnitude.[19]

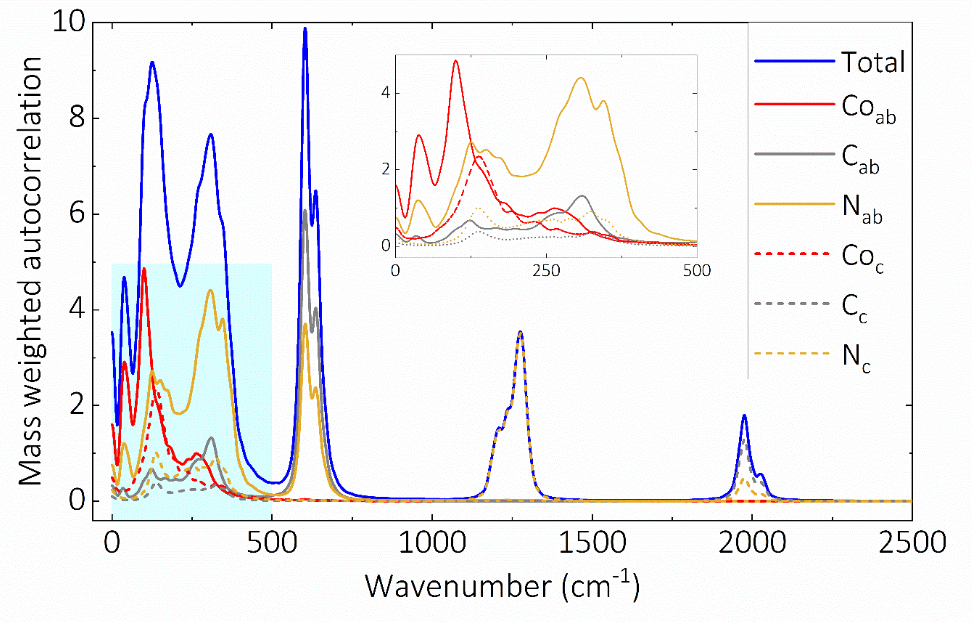

Fig. S11. Calculated vibrational spectra of CoNCN showing the projected vibrational modes over single atoms and directions. All vibrational peaks in the range 300-900 cm^{-1} correspond to vibrational modes arising from the CoNCN matrix.

5 OPERANDO XAS

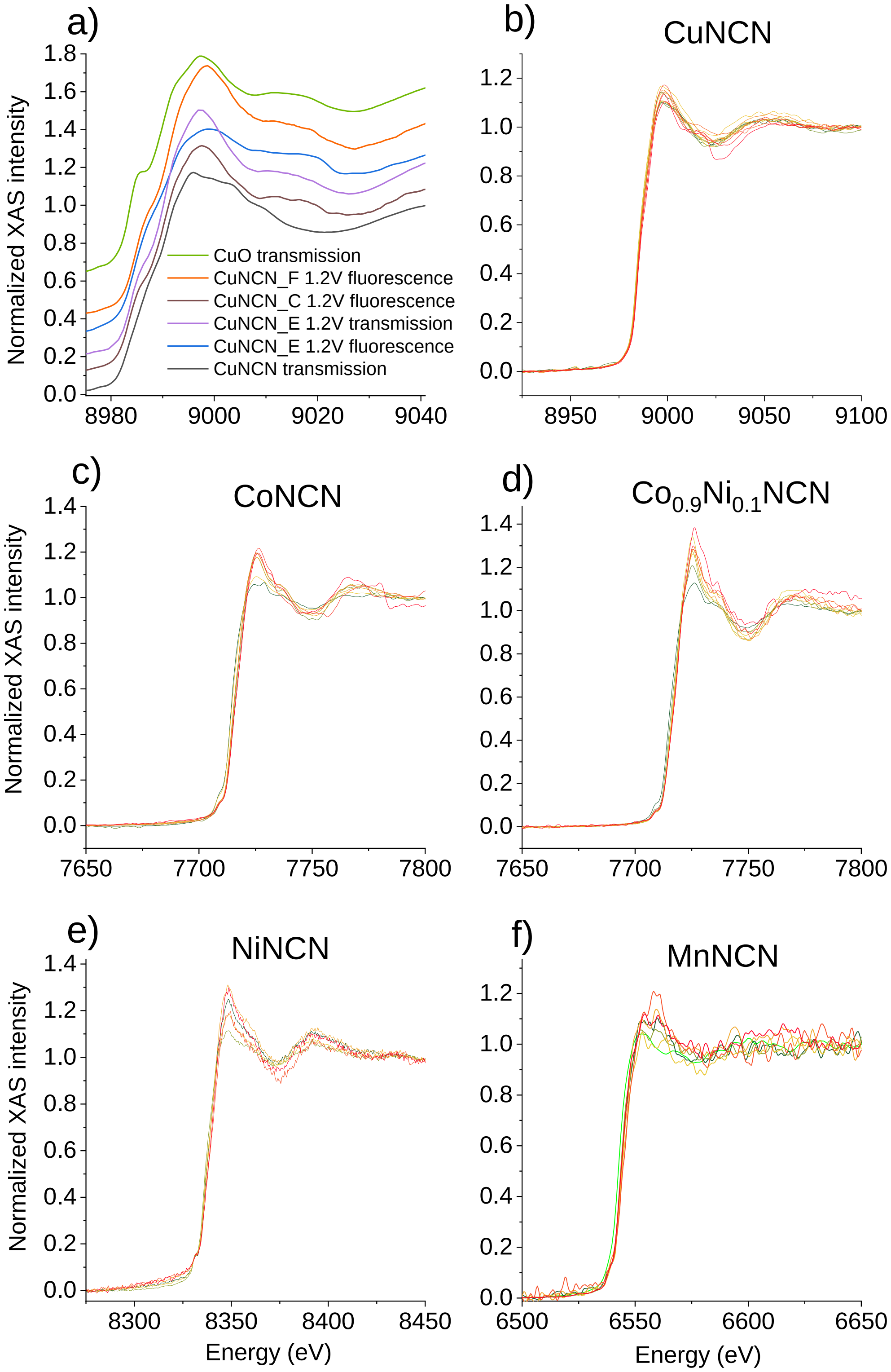

Fig. S12. (a) The change of CuNCN XANES at high potential (1.2 V) was reproducibly detected on 3 different electrodes and also measured in both fluorescence and transmission mode. The latter was achieved after transferring the washed coating onto a Kapton film after the *operando* experiment. (b) – (f) Operando XAS spectra of MNCN modified SPEs. Each spectrum is merged from accumulations at a given applied potential starting from 0.0 V (green) via yellow to 1.2 V (red). The observed variations do not follow a distinct trend and disturbance of bubble formation causes random intensity jumps. A horizontal edge energy shift may be apparent to the eye but is not confirmed by the determination of the first derivative maximum. In fact this minor trend is more likely related to saturation of the detector, which is indicated by the isosbestic point at the normalized absorption intensity of 1.0.

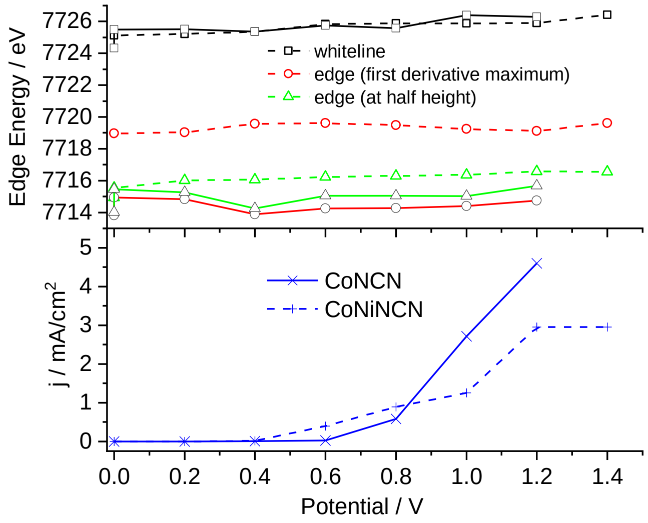

Fig. S13. Top: Energies of whiteline peak and absorption edge versus potential. Bottom: Current density versus potential (full lines: CoNCN, dashed lines: $Co_{0.9}Ni_{0.1}NCN$). No significantly correlated edge shift (less than 1 eV) is observed during the potential scan up to 1.4 V. Oxygen evolution onset is observed above 0.6 V.

6 OPERANDO RAMAN SPECTROSCOPY

Raw data was averaged and smoothed depending on the accumulated signal intensity and scattering properties of the sample. Spectra represented in overlay plots are shifted by a vertical offset to increase visibility. The peak at 265 cm^{-1} cannot be attributed to the catalyst or side products from synthesis, as it is neither found in any reference, nor in pristine, pre- or post-catalytic *ex situ* measurements reported elsewhere. As this signal also occurred in spectra with very low overall scattering intensity, it is unlikely to be related to MNCN and is thus rather a spectral artefact or a phenomenon restricted to the operando conditions or the specific setup.

6.1 CoNiNCN

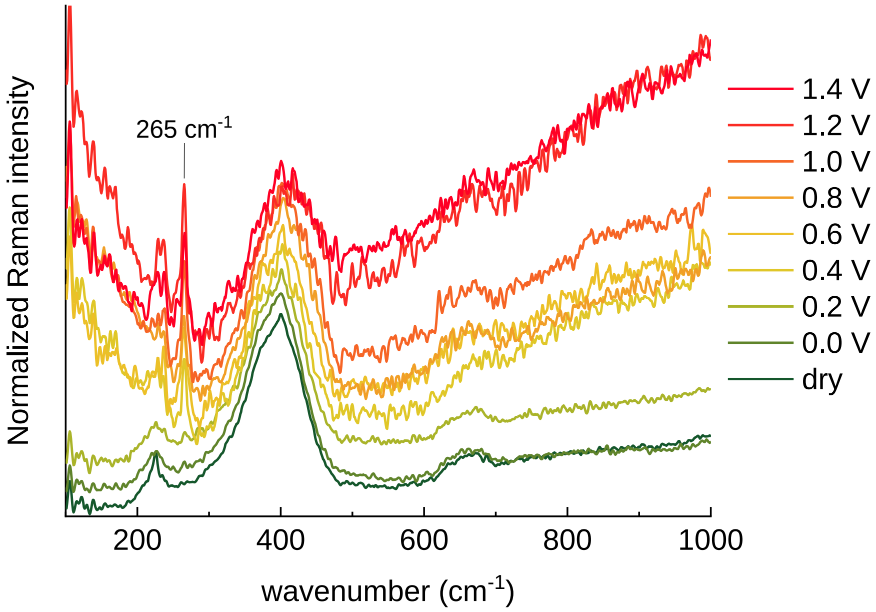

Fig. S14. Operando Raman spectra of 10 µL loading $Co_{0.9}Ni_{0.1}NCN$@Nafion coated SPE. The most characteristic MNCN peak at 400 cm^{-1} is well visible and the peaks at 220 cm^{-1} and 650 cm^{-1} are also attributed to $Co_{0.9}Ni_{0.1}NCN$ (raw data were smoothed by 5 points adjacent averaging, the baseline was subtracted and intensity was normalized to the main peak at 400 cm^{-1}). The peak at 265 cm^{-1} is a frequently occurring measurement artefact (see above).

6.2 NiNCN

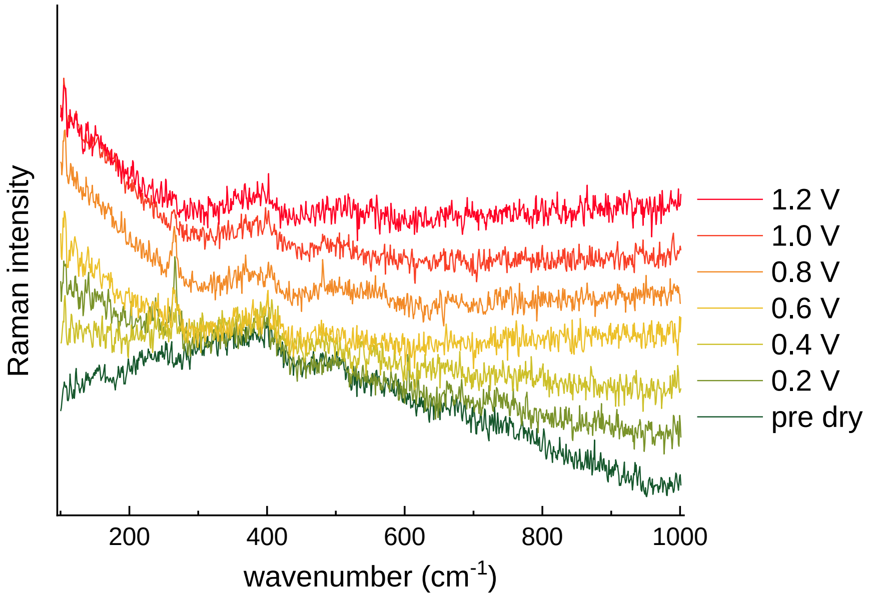

Fig. S15. Operando Raman spectra of 10 µL loading NiNCN@Nafion coated SPE. Very weak scattering properties only permitted detection of the characteristic MNCN peak at 400 cm^{-1}.

6.3 MnNCN

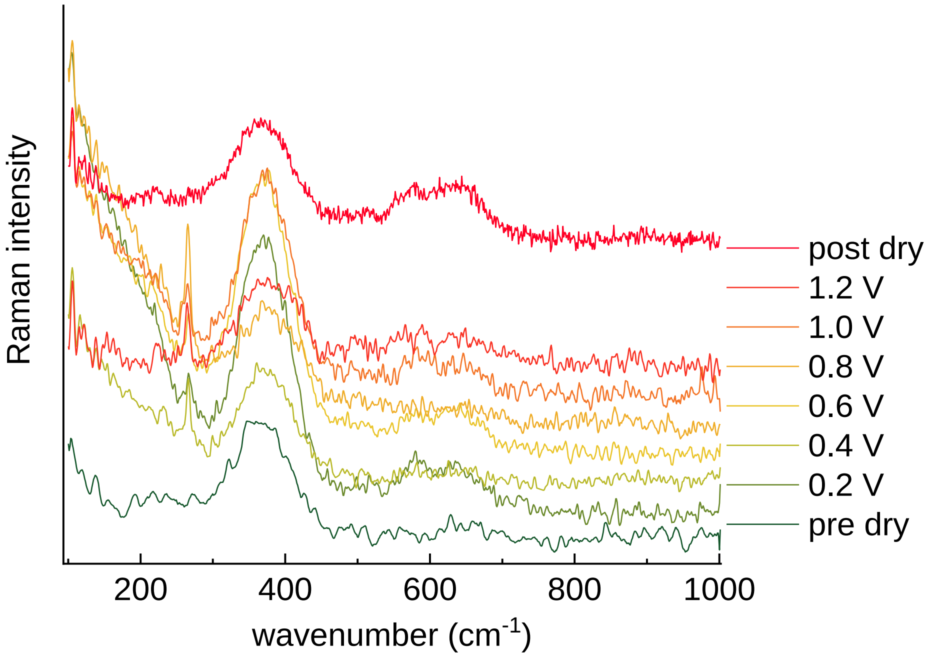

Fig. S16. Operando Raman spectra of 10 µL loading MnNCN@Nafion coated SPE. The characteristic MNCN peak at 400 cm^{-1} is well visible (raw data were smoothed by 5 points adjacent averaging, the baseline was subtracted, and intensity was normalized to the main peak at 400 cm^{-1}). The peak at 265 cm^{-1} is a frequently occurring measurement artefact.

6.4 CuNCN

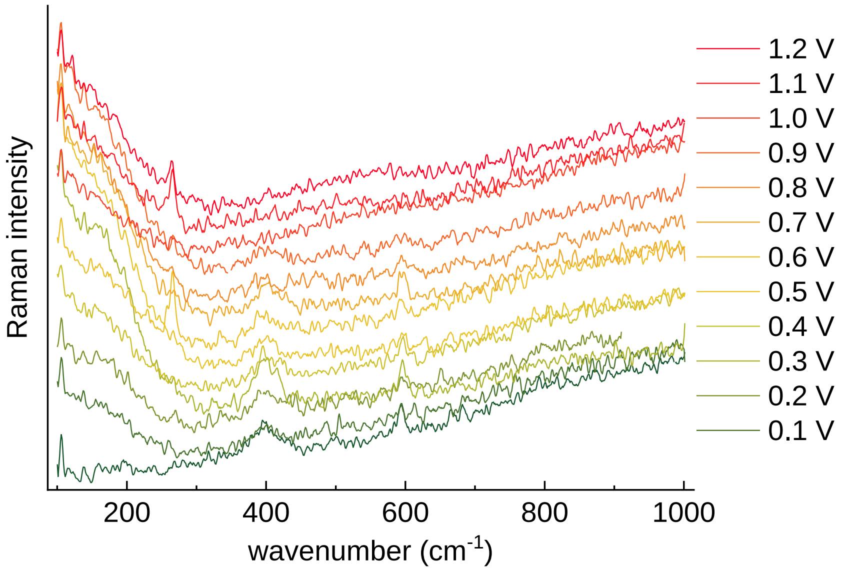

Fig. S17. Operando Raman spectra of 10 µL loading CuNCN@Nafion coated SPE (CuO peaks were not detectable due to low overall scattering intensity).

7 REFERENCES

(1) Liu, X.; Krott, M.; Müller, P.; Hu, C.; Lueken, H.; Dronskowski, R. *Inorg. Chem.* **2005**, *44*, 3001–3003.

(2) Krott, M.; Liu, X.; Müller, P.; Dronskowski, R. *J. Solid State Chem.* **2007**, *180*, 307–312.

(3) Krott, M.; Liu, X.; Fokwa, B. P. T.; Speldrich, M.; Lueken, H.; Dronskowski, R. *Inorg. Chem.* **2007**, *46*, 2204–2207.

(4) Krott, M., Ph.D. Thesis, RWTH Aachen University, Aachen, **2009**.

(5) Ressnig, D.; Clavel, G.; Scharnagl, N.; Antonietti, M. *Part. Part. Syst. Char.* **2014**, *31*, 557–560.

(6) Ressnig, D., Ph.D. Thesis, Universität Potsdam, Max Planck Society, **2014**.

(7) Ressnig, D.; Shalom, M.; Patscheider, J.; Moré, R.; Evangelisti, F.; Antonietti, M.; Patzke, G. R. *J. Mater. Chem. A* **2015**, *3*, 5072–5082.

(8) Koziej, D.; Krumeich, F.; Nesper, R.; Niederberger, M. *J. Mater. Chem.* **2009**, *19*, 5122.

(9) Bard, A.J.; Faulkner, L.R. *Electrochemical Methods-Fundamentals and Applications*, 2nd Edition Chapter 9; John Wiley & Sons, Inc: New York, **2000**.

(10) Reckeweg, O.; Simon, A. *Z. Naturforsch. B* **2003**, *58*, 1097–1104.

(11) Hutter, J.; Iannuzzi, M.; Schiffmann, F.; VandeVondele, J. *Wiley Interdiscip. Rev.-Comput. Mol. Sci.* **2014**, *4*, 15–25.

(12) VandeVondele, J.; Krack, M.; Mohamed, F.; Parrinello, M.; Chassaing, T.; Hutter, J. *Comput. Phys. Commun.* **2005**, *167*, 103–128.

(13) VandeVondele, J.; Hutter, J. *J. Chem. Phys.* **2007**, *127*, 114105.

(14) Goedecker, S.; Teter, M.; Hutter, J. *Phys. Rev. B* **1996**, *54*, 1703.

(15) Nosé, S. *J. Chem. Phys.* **1984**, *81*, 511–519.

(16) Nosé, S. *Mol. Phys.* **1984**, *52*, 255–268.

(17) Brehm, M.; Kirchner, B. *J. Chem. Inf. Model.* **2011**, *51*, 2007–2023.

(18) Thomas, M.; Brehm, M.; Fligg, R.; Vöhringer, P.; Kirchner, B. *PCCP* **2013**, *15*, 6608–6622.

(19) Alecu, I. M.; Zheng, J.; Zhao, Y.; Truhlar, D. G. *J. Chem. Theory Comput.* **2010**, *6*, 2872–2887.